



**HAL**  
open science

# Electromagnetic modeling of damaged fiber-reinforced laminates

Zicheng Liu, Changyou Li, Yu Zhong, Dominique Lesselier

► **To cite this version:**

Zicheng Liu, Changyou Li, Yu Zhong, Dominique Lesselier. Electromagnetic modeling of damaged fiber-reinforced laminates. *Journal of Computational Physics*, 2020, 409 (109318), 15 pp. 10.1016/j.jcp.2020.109318 . hal-02200588

**HAL Id: hal-02200588**

**<https://centralesupelec.hal.science/hal-02200588>**

Submitted on 7 Mar 2022

**HAL** is a multi-disciplinary open access archive for the deposit and dissemination of scientific research documents, whether they are published or not. The documents may come from teaching and research institutions in France or abroad, or from public or private research centers.

L'archive ouverte pluridisciplinaire **HAL**, est destinée au dépôt et à la diffusion de documents scientifiques de niveau recherche, publiés ou non, émanant des établissements d'enseignement et de recherche français ou étrangers, des laboratoires publics ou privés.



Distributed under a Creative Commons Attribution - NonCommercial 4.0 International License



Contents lists available at ScienceDirect

## Journal of Computational Physics

journal homepage: [www.elsevier.com/locate/jcp](http://www.elsevier.com/locate/jcp)



# Electromagnetic modeling of damaged fiber-reinforced laminates

Zicheng Liu<sup>a,b,\*</sup>, Changyou Li<sup>c</sup>, Yu Zhong<sup>d</sup>, Dominique Lesselier<sup>a</sup>

<sup>a</sup>Laboratoire des Signaux et Systèmes, UMR8506 (CNRS-CentraleSupélec-Université Paris-Sud), Université Paris-Saclay, Gif-sur-Yvette cedex 91192, France

<sup>b</sup>Chaire C2M, LTCl, Télécom ParisTech, Université Paris-Saclay, Paris 75013, France.

<sup>c</sup>Department of Electronic Engineering, Northwestern Polytechnical University, Xi'an, 710129, China

<sup>d</sup>A\*STAR, Institute of High Performance Computing, Singapore, 138632, Singapore

### ARTICLE INFO

Article history:

**Keywords:** nondestructive testing, array scanning method, multipole method, damaged periodic structure, fibered laminates, Green's function, equivalence theory, plane-wave expansion, cylindrical-wave expansion

### ABSTRACT

As a prerequisite to nondestructive testing of damaged fibered laminates, the Green's function, corresponding with an undamaged structure, and the electromagnetic fields associated with the damaged one are investigated herein. For the undamaged fibered laminate, benefiting from the periodicity of the fibers within each layer, the field solution follows the scattering-matrix-based method using the Floquet theorem. Yet, the periodicity is destroyed by the analytical source (for the Green's function) or by damages, and the Floquet theorem cannot be directly applied to compute the associated scattering matrices. The array scanning method is introduced to that effect. Inserting fictitious sources to get a quasi-periodic source array, the modeling approach for undamaged laminates can be used to compute the field with the source array, the integration of which cancels the effects of the fictitious sources and yields the Green's function. With the multipole method, field disturbances by damages, which include missing, displaced, shrunk, and expanded fibers and circular inclusions inside fibers, are accurately modeled by setting equivalent sources inside sound fibers, and the array scanning method applies. Modeling accuracy and efficiency of the approaches are illustrated by numerical simulations.

## 1. Introduction

Fiber-reinforced laminates are widely used in aerospace and automotive industries due to advantages in stiffness and weight. Each layer of the laminate is composed of a planar slab and an embedded periodic fiber array. Fiber material might be glass or graphite, and the slab itself is usually made of epoxy or polyester. Stacking the reinforced

\*Corresponding author at Chaire C2M, LTCl, Télécom ParisTech, 46 rue Barrault, 75013 Paris. E-mail address: [zicheng.liu@telecom-paristech.fr](mailto:zicheng.liu@telecom-paristech.fr)

slabs yields the concerned structure and, to provide strength along various directions, fiber orientations in different layers usually differ. Nondestructive testing of potential damages inside is necessary in order to ensure reliability and safety. Electromagnetic (EM) means can be used to that effect because of broad applicability on both conductive [1] and dielectric [2] composites. Correspondingly, accurate modeling and high-resolution imaging methods are requested to guarantee the detection performances, the former rarely reported in literature and being focused onto in the present contribution.

As indicated, modeling of damaged and undamaged laminates is required to better study impacts of damages and configure the testing systems, but may not be easily handled by commercial softwares (e.g., COMSOL) as the boundary conditions are not clear due to the periodicity at different directions in each layer. Efforts have been made by (some of) present authors. Without damages, the modeling approach refers to works in [3] where fields near slab boundaries are expanded into plane-wave expansions (PWEs) in order to facilitate modes matching, and the multipole method [4] is adopted to analyze the fiber array. However, the applicability of such methods to the disorganized structure is prevented by the fact that the periodicities are destroyed. Approximated field solutions can be provided by brute-force codes running FDTD [5] or FEM [6] methods. Since regions near the damages are those of main interest, a truncated model (a cell) of the laminate centered on the damages is often investigated. To guarantee accuracy, testing the field convergence is needed by enlarging the cell, i.e., increasing the truncation size. A similar methodology is followed in our previous work [7], save periodic conditions being set at the end sides of the cell to fabricate a new, fictitious periodic structure; then, quasi-periodic theories apply. But the unknown approximation errors (due to lack of the true solution) and possibly heavy computational cost in case of low-loss materials show the necessity of developing a more sophisticate modeling.

Contributions have been made by authors in [8] on efficiently and accurately modeling damaged single-layer laminates with missing, displaced, shrunk, and expanded fibers and circular inclusions inside fibers. Defects are electromagnetically equivalent to sources within the initially organized fibers by reformulating the changed fiber boundary conditions or via application of Graf's addition theorem. Then the field solution is a summation of responses due to the exterior emitting source and to the equivalent ones. The former is obtained with the method dealing with undamaged structures [3]. The latter is obtained via the array scanning method (ASM) [9] where a phased source array is assumed so that quasi-periodic theories become applicable and the final solution results from integration over the first Brillouin zone.

In this contribution, the equivalence theory is applied on the modeling of damaged multilayer laminates. Treating the concerned damages as equivalent sources, the solution to the illumination of undamaged multilayer laminates by exterior and equivalent sources is required and obtained with the help of scattering matrices [10], which describe mutual scattering between two layers. Playing the key role in both modeling and imaging, the solution to the Green's function, i.e., the response to a line source in 2-D cases, is also explored following the same computational approach as for equivalent sources.

Representing the field in the whole region by PWEs or CWEs (short for cylindrical-wave expansions), the above solution is achieved through the retrieval of expansion coefficients, for which PWEs and CWEs are truncated and

the truncation size should be properly set. A numerical strategy, which makes use of the knowledge that PWEs and CWEs should yield the same field solution in the commonly supported region, is proposed, while the possible different structures (in terms of material and of geometry) of layers are considered to yield the correspondingly different truncation sizes.

The contribution is structured as follows. Notations and configurations are introduced in Section 2, the undamaged structure being of first concern. The exterior illumination is studied in Section 3. The solution to the Green's function is presented in Section 4. With quantities obtained above, different types of damages are treated as equivalent sources in Section 5 and how to reach the true solution is discussed as well. The truncation number of PWEs and CWEs is the key parameter in the modeling. A numerical strategy is presented in Section 6 to adaptively select the optimal value. The numerical analysis is considered in Section 7 and conclusions are proposed in Section 8. Appendices provide complementary materials.

## 2. Configurations and formulation

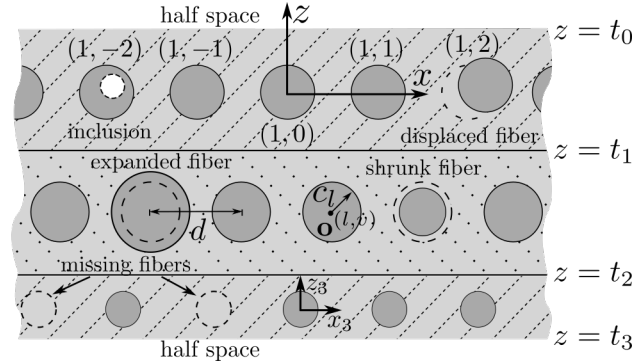


Fig. 1. Sketch of the damaged laminate with defects of concern,  $L = 3$ .

The description of undamaged laminates goes first, and then the one of concerned damages. The structure of the multilayer laminate is sketched in Fig. 1, where it is sandwiched by two half spaces at top and bottom, each layer of the laminate being made by periodically inserting similarly-orientated fibers inside a planar slab. The composition of different layers can differ w.r.t. fiber radius, slab thickness and materials. The fiber periods are to be the same here.

Assume  $L$  layers are stacked on one another. Labeling them with integers from 1 to  $L$ , the upper and lower half spaces are indexed by 0 and  $L + 1$ , respectively. Setting the origin of the global coordinate system at the center of a fiber in the 1st layer, the local coordinate system for the  $l$ -th layer is defined by setting the origin at the fiber center  $\mathbf{o}^{(l,0)}$  with global coordinates  $(o_x^{(l,0)}, o_z^{(l,0)})$ ,  $t_{l+1} < o_z^{(l,0)} < t_l$ ,  $-d/2 < o_x^{(l,0)} \leq d/2$ ,  $l = 1, \dots, L$ , the plane  $z = t_l$  denoting the lower boundary of the  $l$ -th layer and  $d$  the fiber period. Then, the center of fibers in the  $l$ -th layer has local coordinates  $(x_l, z_l) = (vd, 0)$ ,  $v \in \mathbb{Z}$ , based on which fibers in the  $l$ -th layer are labeled by integer couples  $(l, v)$ . Remark that the subscript of  $x$  and  $z$  indicates the coordinate system, i.e., “ $l$ ” stands for the local coordinate system of the  $l$ -th layer.

All materials, including the one in the inclusions, are linear, isotropic and homogeneous. Fiber and slab materials are layer-dependent, characterized by relative permittivities  $\epsilon_j^l$  (complex value for lossy materials) and relative permeabilities  $\mu_j^l$ ,  $j = "f"$  for fiber and  $"s"$  for slab.

Consider now the damaged laminate. Indexes of damaged fibers compose the set  $\mathbb{D}$ , i.e., the  $v$ -th fiber in the  $l$ -th layer is damaged if  $(l, v) \in \mathbb{D}$ . A tilde is put above the corresponding notations to denote the damaged status. One respectively denotes the center and radius of the  $(l, v)$ -th fiber by  $\mathbf{o}^{(l,v)}$  and  $c_l$  for the undamaged laminate, the local coordinates of  $\tilde{\mathbf{o}}^{(l,v)} \neq (vd, 0)$  for displaced fibers and  $\tilde{c}^{(l,v)} \neq c_l$  for shrunk/expanded ones. A circular inclusion is configured by its center  $\tilde{\mathbf{o}}^{(l,v)}$  and radius  $\tilde{c}^{(l,v)}$ , with a bar above corresponding notations. Without loss of generality, half spaces and inclusions are assumed filled by air and missing fibers are "fibers" sharing the same material with the background slab.

With time-dependence  $\exp(-i\omega t)$ ,  $i$  imaginary unit,  $\omega$  angular frequency, the incident waves considered are either time-harmonic plane waves of  $(x, z)$  plane of incidence or line sources orientated along the  $y$  axis, with either TM or TE field polarization. This configuration leads to a two-dimensional scalar scattering problem, which means only the  $y$ -component of electric field (for TM) or magnetic field (for TE) needs to be tackled.

### 3. Electromagnetic modeling of undamaged laminates

The modeling of damaged laminates is based on the analysis of the corresponding undamaged ones. For completeness, this Section revisits the modeling approach [10] for undamaged laminates illuminated by a planar wave (considering that other types of sources might be analyzed by exploiting their PWEs [11, 12]).

Analyzing wave propagations within each layer through the combination of multipole method and field matching on boundaries, scattering behaviors in different layers are linked by scattering matrices (rather than possibly ill-conditioned transfer matrices [10]), which are computed according to a recursive scheme.

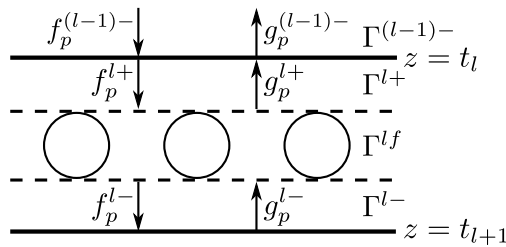


Fig. 2. Coefficients of plane-wave expansions in the  $l$ -th layer for upgoing and down-going waves.

As shown in Fig. 2, for the  $l$ -th layer, the fiber array divides the layer into three slices, region above the array, region below it, and the array itself, denoted by  $\Gamma^{l+}$ ,  $\Gamma^{l-}$  and  $\Gamma^{lf}$ , respectively. Due to the periodicity of the structure, the Floquet theorem applies and the total field follows a pseudo-periodic distribution, i.e.,  $V(\mathbf{r} + d\hat{x}) = V(\mathbf{r})e^{i\alpha_0 d}$ , where  $V$  stands for the  $y$ -component of the E- or H-field depending upon the wave polarization,  $\mathbf{r}$  denotes the observation position,  $\hat{x}$  is the unit vector along the  $x$  axis, and  $\alpha_0 = k_s^0 \sin \theta^{inc}$ ,  $k_s^0$  being the wavenumber of the upper half space and  $\theta^{inc}$  being the incident angle of the plane wave measured counter-clockwise from the  $z$  axis.

The pseudo-periodic property of  $V$  yields its representation in PWEs [13]. For the region of  $\Gamma^{l+}$  and  $\Gamma^{l-}$ , the expansion is with coefficients  $f_p^{l+}$ ,  $g_p^{l+}$  and  $f_p^{l-}$ ,  $g_p^{l-}$ , respectively. The subscript “ $p$ ” denotes the expansion order and “ $g$ ”, “ $f$ ” stand for field components propagating along the  $z$ -axis and the opposite direction, respectively. Thus, in the local coordinate system,

$$V(\mathbf{r}) = \sum_{p \in \mathbb{Z}} \left[ f_p^{l\pm} e^{-i\beta_p^l z_l} + g_p^{l\pm} e^{i\beta_p^l z_l} \right] e^{i\alpha_p x_l}, \quad \mathbf{r} \in \Gamma^{l\pm}, \quad (1)$$

where  $\alpha_p = \alpha_0 + p2\pi/d$ ,  $\beta_p^l = \sqrt{(k_s^l)^2 - \alpha_p^2}$ .

Matching fields at the slab boundary  $z = t_l$ , expansion coefficients at the two sides of this boundary are related as

$$\begin{bmatrix} \mathbf{f}^{l+} \\ \mathbf{g}^{(l-1)-} \end{bmatrix} = \begin{bmatrix} \mathcal{E}_l^1 & \mathcal{E}_l^2 \\ \mathcal{E}_l^3 & \mathcal{E}_l^4 \end{bmatrix} \begin{bmatrix} \mathbf{f}^{(l-1)-} \\ \mathbf{g}^{l+} \end{bmatrix}. \quad (2)$$

where  $\mathbf{f}^{l\pm} = [f_p^{l\pm}]$ ,  $\mathbf{g}^{l\pm} = [g_p^{l\pm}]$ , and the definition of  $\mathcal{E}_l^u$ ,  $u = 1, 2, 3, 4$ , is given in Appendix A. Since  $\mathbf{f}^{l+}$ ,  $\mathbf{g}^{(l-1)-}$  stand for waves scattered by the boundary and  $\mathbf{f}^{(l-1)-}$ ,  $\mathbf{g}^{l+}$  for incident ones, the matrix composed by  $\mathcal{E}_l^u$  indicates the scattering property of the slab boundary at  $z = t_l$ . Such relation w.r.t. the fiber array is also obtained with the multipole method [4].

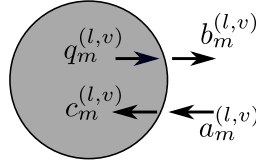


**Fig. 3. Field representation by cylindrical-wave expansions in the  $(l, v)$ -th fiber.**

Expressing the total field in the vicinity of and inside the  $(l, v)$ -th fiber in cylindrical-wave expansions (CWEs),

$$V(\mathbf{r}) = \sum_{m \in \mathbb{Z}} \left[ a_m^{(l,v)} \varphi_m^J(k_s^l, \mathbf{r}_{(l,v)}) + b_m^{(l,v)} \varphi_m^{H(1)}(k_s^l, \mathbf{r}_{(l,v)}) \right], \quad (3a)$$

$$V(\mathbf{r}) = \sum_{m \in \mathbb{Z}} \left[ c_m^{(l,v)} \varphi_m^J(k_j^l, \mathbf{r}_{(l,v)}) + q_m^{(l,v)} \varphi_m^{H(1)}(k_j^l, \mathbf{r}_{(l,v)}) \right], \quad (3b)$$

where  $\mathbf{r}_{(l,v)}$  is the relative position of the observation point  $\mathbf{r}$  w.r.t. the fiber center  $\mathbf{o}^{(l,v)}$ , i.e.,  $\mathbf{r}_{(l,v)} = \mathbf{r} - \mathbf{o}^{(l,v)}$ . Denoting  $(r_{(l,v)}, \theta_{(l,v)})$  as the polar coordinates of  $\mathbf{r}_{(l,v)}$ ,  $\varphi_m^Z(k_j^l, \mathbf{r}_{(l,v)}) = Z_m(k_j, r_{(l,v)}) \exp(im\theta_{(l,v)})$ , where  $Z = J$  stands for the Bessel function and  $Z = H^{(1)}$  for the first-kind Hankel function. The coefficients of the CWEs are sketched in Fig. 3. While the coefficient of  $c_m^{(l,v)}$  and  $a_m^{(l,v)}$  stands for the wave propagating towards the fiber center,  $b_m^{(l,v)}$  and  $q_m^{(l,v)}$  denote the field scattered by the fiber and the inner source (e.g., the analytical line source inside the fiber for the scalar Green's function), respectively.

The total field outside fibers of each layer is a summation of fields scattered by the corresponding upper and lower slab boundaries with PWE coefficients  $f_p^{l+}$  and  $g_p^{l-}$  and fields scattered by all fibers with CWE coefficients  $b_m^{(l,v)}$ . The CWE representation of the latter is with the identity

$$\sum_{v \in \mathbb{Z}} \sum_{m \in \mathbb{Z}} b_m^{(l,0)} e^{i\alpha_0 v d} \varphi_m^{H(1)}(k_s^l, \mathbf{r}_{(l,0)} - v d \hat{x}) = \sum_{p \in \mathbb{Z}} \left( \sum_{m \in \mathbb{Z}} K_{m,p}^{l\pm} b_m^{(l,0)} \right) e^{i(\alpha_p x_l \pm \beta_p^l z_l)}, \quad (4)$$

where  $K_{m,p}^{l\pm} = 2(-i)^m \exp(\pm im\theta_p^l) / (d\beta_p^l)$ ,  $\cos\theta_p^l = \alpha_p/k_s^l$ , and the Floquet theorem has been applied with  $b_m^{(l,v)} = b_m^{(l,0)} e^{i\alpha_0 v d}$ . Thus, the total field in the  $l$ -th layer is expressed as a PWE as

$$V(\mathbf{r}) = \sum_{p \in \mathbb{Z}} e^{i\alpha_p x_l} \left[ f_p^{l+} e^{-i\beta_p^l z_l} + g_p^{l-} e^{i\beta_p^l z_l} + \left( \sum_{m \in \mathbb{Z}} K_{m,p}^{l\pm} b_m^{(l,0)} \right) e^{\pm i\beta_p^l z_l} \right], \quad (5)$$

the matrix form of which is

$$V(\mathbf{r}) = \Xi^{l-} \mathbf{f}^{l+} + \Xi^{l+} \mathbf{g}^{l-} + \Xi^{l\pm} \mathbf{K}^{l\pm} \mathbf{b}^{(l,0)}, \quad (6)$$

where  $\Xi^{l\pm} = [e^{i(\alpha_p x_l \pm \beta_p^l z_l)}]$ ,  $\mathbf{K}^{l\pm} = [K_{m,p}^{l\pm}]$ . Signs + and - are applicable in the region of  $z_l \geq 0$  and  $z_l < 0$ , respectively, for  $\Xi^{l\pm}$  and  $\mathbf{K}^{l\pm}$ . The relationship between  $b_m^{(l,0)}$ ,  $f_p^{l+}$ ,  $g_p^{l-}$  is exploited by analyzing the scattering behaviors of the fiber array.

With the field representation as CWEs in Eq. (3), the fiber boundary conditions yield the linear relations of CWE coefficients,

$$b_m^{(l,v)} = R_m^l a_m^{(l,v)} + T_m^l q_m^{(l,v)}, \quad (7a)$$

$$c_m^{(l,v)} = T_m^{l'} a_m^{(l,v)} + R_m^{l'} q_m^{(l,v)}, \quad (7b)$$

where  $R_m^l$ ,  $R_m^{l'}$ ,  $T_m^l$ ,  $T_m^{l'}$  are reflection or transmission coefficients defined in Appendix A. Remark that  $q_m^{(l,v)}$  equals 0 since no inner source exists. Together with the so-called Rayleigh identities [14],

$$a_m^{(l,0)} = \sum_{n \in \mathbb{Z}} S_{m-n}^l b_n^{(l,0)} + \sum_{p \in \mathbb{Z}} \left( J_{m,p}^{l+} \mathbf{g}^{l-} + J_{m,p}^{l-} \mathbf{f}^{l+} \right), \quad (8)$$

which is obtained with the Jacobi-Anger expansion [15] and application of the Graf's addition theorem [15], the expression of  $b_m^{(l,0)}$  as a function of  $f_p^{l+}$  and  $g_p^{l-}$  is written as

$$\mathbf{b}^{(l,0)} = \left( \mathbf{I} - \mathbf{R}^l \mathbf{S}^l \right)^{-1} \mathbf{R}^l \left( \mathbf{J}^{l+} \mathbf{g}^{l-} + \mathbf{J}^{l-} \mathbf{f}^{l+} \right), \quad (9)$$

where  $\mathbf{I}$  is the identity matrix,  $\mathbf{b}^{(l,0)} = [b_m^{(l,0)}]$ ,  $\mathbf{R}^l = \text{diag}\{R_m^l\}$ ,  $\mathbf{S}^l = [S_{m-n}^l]$ ,  $\mathbf{J}^{l\pm} = [J_{m,p}^{l\pm}]$ ,  $J_{m,p}^{l\pm} = (i)^m \exp(\mp im\theta_p^l)$  and  $S_{m-n}^l$  is the lattice sum defined as

$$S_m^l = \sum_{v \in \mathbb{Z} \setminus \{0\}} H_m^{(1)}(k_s^l |v| d) e^{i(\alpha_0 l d - m \arg(v))}, \quad (10)$$

which enjoys a fast convergence about  $v$  for lossy slabs whereas the computation approaches in [16, 17] apply for lossless cases.

The substitution of Eq. (9) into Eq. (6) leads to  $V$  as a function of PWE coefficients  $\mathbf{f}^{l+}$  and  $\mathbf{g}^{l-}$ . Together with Eq. (1), the scattering matrix of the fiber array is obtained and described as

$$\begin{bmatrix} \mathbf{f}^{l-} \\ \mathbf{g}^{l+} \end{bmatrix} = \begin{bmatrix} \mathcal{F}_l^1 & \mathcal{F}_l^2 \\ \mathcal{F}_l^3 & \mathcal{F}_l^4 \end{bmatrix} \begin{bmatrix} \mathbf{f}^{l+} \\ \mathbf{g}^{l-} \end{bmatrix}, \quad (11)$$

where  $\mathcal{F}_l^1 = \mathbf{I} + \Omega^{l-} \mathbf{R}^l \mathbf{J}^{l-}$ ,  $\mathcal{F}_l^2 = \Omega^{l-} \mathbf{R}^l \mathbf{J}^{l+}$ ,  $\mathcal{F}_l^3 = \Omega^{l+} \mathbf{R}^l \mathbf{J}^{l-}$ ,  $\mathcal{F}_l^4 = \mathbf{I} + \Omega^{l+} \mathbf{R}^l \mathbf{J}^{l+}$ ,  $\Omega^{l\pm} = \mathbf{K}^{l\pm} (\mathbf{I} - \mathbf{R}^l \mathbf{S}^l)^{-1}$ . Then, the scattering effects of the fiber array are equivalent to a slab boundary with the scattering matrix defined by  $\mathcal{F}_l^u$ ,  $u = 1, 2, 3, 4$ .

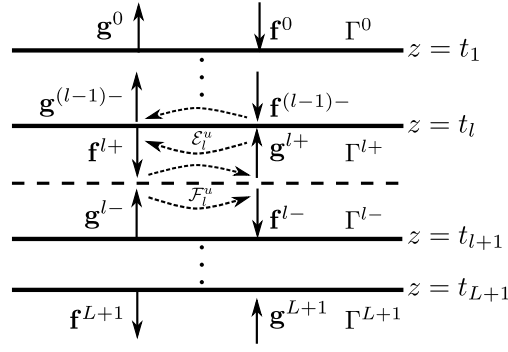


**Fig. 4.** Equivalence of fiber arrays as planar boundaries with scattering matrices  $\mathcal{E}_l^u$  and  $\mathcal{F}_l^u$ ,  $u = 1, 2, 3, 4$ , defined by Eq. (2) and (11).

Representing the equivalent boundary by the slashed line, the sketch in Fig. 2 is reformulated as Fig. 4. Following the recursive scheme in [10], scattering matrices linking PWE coefficients in any two slices are computed. Based on the computed scattering matrices, the PWE and CWE coefficients can be solved for.

The scattering matrix linking the slice  $\Gamma^0$  and  $\Gamma^{l\pm}$  is defined by

$$\begin{bmatrix} \mathbf{f}^{l\pm} \\ \mathbf{g}^0 \end{bmatrix} = \begin{bmatrix} \mathcal{A}_0^{l\pm} & \mathcal{B}_0^{l\pm} \\ \mathcal{C}_0^{l\pm} & \mathcal{D}_0^{l\pm} \end{bmatrix} \begin{bmatrix} \mathbf{f}^0 \\ \mathbf{g}^{l\pm} \end{bmatrix}, \quad (12)$$

and the one linking  $\Gamma^{l\pm}$  and  $\Gamma^{L+1}$  by

$$\begin{bmatrix} \mathbf{f}^{L+1} \\ \mathbf{g}^{l\pm} \end{bmatrix} = \begin{bmatrix} \mathcal{A}_{l\pm}^{L+1} & \mathcal{B}_{l\pm}^{L+1} \\ \mathcal{C}_{l\pm}^{L+1} & \mathcal{D}_{l\pm}^{L+1} \end{bmatrix} \begin{bmatrix} \mathbf{f}^{l\pm} \\ \mathbf{g}^{L+1} \end{bmatrix}. \quad (13)$$

Considering the coefficient vector  $\mathbf{f}^0$  (PWE coefficients of the incident wave) is known and  $\mathbf{g}^{L+1} = \mathbf{0}$  due to no incident field from the bottom, one has equations

$$\mathbf{g}^{l\pm} = \mathcal{C}_{l\pm}^{L+1} \mathbf{f}^{l\pm}, \quad (14a)$$

$$\mathbf{f}^{l\pm} = \mathcal{A}_0^{l\pm} \mathbf{f}^0 + \mathcal{B}_0^{l\pm} \mathbf{g}^{l\pm}, \quad (14b)$$

which yield the solution of  $\mathbf{f}^{l\pm}$  and  $\mathbf{g}^{l\pm}$  as

$$\mathbf{f}^{l\pm} = \left( \mathbf{I} - \mathcal{B}_0^{l\pm} \mathcal{C}_{l\pm}^{L+1} \right)^{-1} \mathcal{A}_0^{l\pm} \mathbf{f}^0, \quad (15a)$$

$$\mathbf{g}^{l\pm} = \mathcal{C}_{l\pm}^{L+1} \mathbf{f}^{l\pm}. \quad (15b)$$

When  $l = L + 1$ , one has  $\mathbf{f}^{L+1} = \mathcal{A}_0^{L+1} \mathbf{f}^0$  and  $\mathbf{g}^0 = \mathcal{C}_0^{L+1} \mathbf{f}^0$ . CWE coefficients are computed by substituting  $\mathbf{f}^{l\pm}$  and  $\mathbf{g}^{l\pm}$  into Eq. (8) and (9). With PWE and CWE coefficients, the full-field solution is achieved.

#### 4. The Green's function

The Green's function, denoted by  $G(\mathbf{r}, \mathbf{r}_s)$ , is defined as the field solution at  $\mathbf{r}$  when the line source locates at  $\mathbf{r}_s$  and emits field  $H_0^{(1)}(k_j^l r_s)/(4i)$ ,  $j$  being "s" or "f" depending on the source location. Here, due to the role in the modeling of damaged laminates in Section 5, only the case of the line source inside the fiber is considered. Remark that the computation of  $G(\mathbf{r}, \mathbf{r}_s)$  w.r.t. the single-layer laminate has been presented in the authors' earlier works [7].

This Section gives the similar approach but with the combination of the scattering matrix to reach the solution of  $G(\mathbf{r}, \mathbf{r}_s)$  for the multilayer laminate.

Since  $G(\mathbf{r} - vd\hat{x}, \mathbf{r}_s - vd\hat{x}) = G(\mathbf{r}, \mathbf{r}_s)$ , without losing the generality, the line source is assumed located inside the  $(l, 0)$ -th fiber. Section 3 concerns the exterior illumination on the undamaged structure. Thus, the presented modeling approach in Section 3 cannot be applied directly since the source is inside the laminate and destroys the quasi-periodic property of the field distribution.

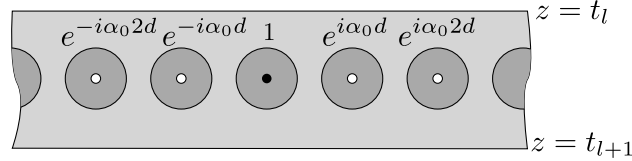


**Fig. 5. Phased line-source array, solid dot standing for the true source and hollow ones for fictitious sources.**

The array scanning method (ASM) overcomes this difficulty by fabricating a phased source array, as shown in Fig. 5. All sources share the same current except the one inside the  $(l, v)$ -th fiber is with phase  $\exp(i\alpha_0 vd)$ , i.e., the true source is with phase 1. With the phased array, the field distribution becomes quasi-periodic and scattering due to the phased array can then be analyzed. Denote the field solution w.r.t. the source array by  $G(\mathbf{r}, \mathbf{r}_s, \alpha_0, \infty)$ . Following the identity

$$\frac{d}{2\pi} \int_{-\pi/d}^{\pi/d} e^{i\alpha_0 vd} d\alpha_0 = \delta_{v,0}, \quad (16)$$

where  $\delta_{v,0}$  equals 1 when  $v = 0$  and 0 otherwise, the impacts of fictitious sources are expected to be canceled after integration over the first Brillouin zone, i.e., the true field solution is

$$G(\mathbf{r}, \mathbf{r}_s) = \frac{d}{2\pi} \int_{-\pi/d}^{\pi/d} G(\mathbf{r}, \mathbf{r}_s, \alpha_0, \infty) d\alpha_0. \quad (17)$$

Numerical methods [18] are used to perform this integration, while the computation of the integrand is introduced next.

Due to the presence of the source array,  $q_m^{(l,v)}$  in Eq. (7) is non-zero. Since the wave radiated by the line source is with expression  $H_0^{(1)}(k_f r_s)/(4i)$ ,  $r_s = |\mathbf{r}_s - \mathbf{o}^{(l,0)}|$ , one has  $q_m^{(l,0)} = J_m(k_f^l |\mathbf{r}_s - \mathbf{o}^{(l,0)}|) \exp(-im \arg(\mathbf{r}_s - \mathbf{o}^{(l,0)})) / 4i$  with the application of the Graf's addition theorem. Thus, Eq. (11) is updated as

$$\begin{bmatrix} \mathbf{f}^{l-} \\ \mathbf{g}^{l+} \end{bmatrix} = \begin{bmatrix} \mathcal{F}_l^1 & \mathcal{F}_l^2 \\ \mathcal{F}_l^3 & \mathcal{F}_l^4 \end{bmatrix} \begin{bmatrix} \mathbf{f}^{l+} \\ \mathbf{g}^{l-} \end{bmatrix} + \begin{bmatrix} \Omega^{l-} \mathbf{T}^l \mathbf{q}^{(l,0)} \\ \Omega^{l+} \mathbf{T}^l \mathbf{q}^{(l,0)} \end{bmatrix}, \quad (18)$$

where  $\mathbf{q}^{(l,0)} = [q_m^{(l,0)}]$ ,  $\mathbf{T}^l = \text{diag}\{T_m^l\}$ . Together with two equations, Eq. (14a) and (14b) ( $\mathbf{f}^0 = \mathbf{0}$  since no exterior source exists), the solution to  $\mathbf{f}^{l\pm}$  and  $\mathbf{g}^{l\pm}$  is obtained as

$$\begin{aligned} \mathbf{g}^{l+} &= \frac{\Theta_{l+} \mathcal{C}_{l-}^{L+1} \Psi_l^{-1} \Omega^{l-} + \Omega^{l+}}{\Xi_l - \Theta_{l+} \mathcal{C}_{l-}^{L+1} \Psi_l^{-1} \Theta_{l-} \mathcal{B}_0^{l+}} \mathbf{T}^l \mathbf{q}^{(l,0)}, \\ \mathbf{f}^{l-} &= \frac{\Theta_{l-} \mathcal{B}_0^{l+} \Xi_l^{-1} \Omega^{l+} + \Omega^{l-}}{\Psi_l - \Theta_{l-} \mathcal{B}_0^{l+} \Xi_l^{-1} \Theta_{l+} \mathcal{C}_{l-}^{L+1}} \mathbf{T}^l \mathbf{q}^{(l,0)}, \\ \mathbf{f}^{l+} &= \mathcal{B}_0^{l+} \mathbf{g}^{l+}, \\ \mathbf{g}^{l-} &= \mathcal{C}_{l-}^{L+1} \mathbf{f}^{l-}, \end{aligned} \quad (19)$$

where  $\Theta_{l\pm} = \mathbf{I} + \Omega^{l\pm} \mathbf{R}^l \mathbf{J}^\pm$ ,  $\Xi_l = \mathbf{I} - \Omega^{l+} \mathbf{R}^l \mathbf{J}^{l-} \mathcal{B}_0^{l+}$ ,  $\Psi_l = \mathbf{I} - \Omega^{l-} \mathbf{R}^l \mathbf{J}^{l+} \mathcal{C}_{l-}^{l+}$ .

With the solution to  $\mathbf{f}^{l\pm}$  and  $\mathbf{g}^{l\pm}$ , as shown in Fig. 4, the laminate can be treated as two parts, layers below and above the  $l$ -th layer. The field solution for the former part is achieved by treating the field component with PWE coefficients  $f_p^{l-}$  as the incident wave and following the computational approach in Section 3. The field solution for the later part is similarly obtained with PWE coefficients  $g_p^{l+}$ .

## 5. Damages modeled as equivalent sources

Through the analysis of the scattering behaviors, the authors found that the field disturbance due to damages, which as already indicated include missing, displaced, expanded, and shrunk fibers and circular inclusions, is equivalent to setting line sources inside the initially organized fibers, on condition that the CWE coefficients of the emitted fields satisfy specific relations. A brief introduction of equivalence theory in [8] is given here for completeness.

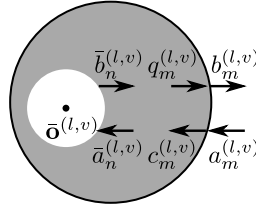


Fig. 6. CWE coefficients inside the fiber with an circular inclusion.

For a circular inclusion, express fields around the inclusion with CWE coefficients shown in Fig. 6. The application of the Graf's addition theorem [7] leads to

$$q_m^{(l,v)} = \sum_{n \in \mathbb{Z}} \varphi_{n-m}^J(k_f^l, \mathbf{o}^{(l,v)} - \bar{\mathbf{o}}^{(l,v)}) \bar{b}_n^{(l,v)}, \quad (20a)$$

$$\bar{a}_m^{(l,v)} = \sum_{n \in \mathbb{Z}} \varphi_{n-m}^J(k_f^l, \bar{\mathbf{o}}^{(l,v)} - \mathbf{o}^{(l,v)}) c_n^{(l,v)}. \quad (20b)$$

Considering the linear relations of CWE coefficients in Eq. (7) and the following one from the boundary condition of the inclusion,

$$\bar{b}_m^{(l,v)} = \bar{R}_m^{(l,v)} \bar{a}_m^{(l,v)}, \quad (21)$$

where  $\bar{R}_m^{(l,v)}$  is similarly defined as  $R_m^{(l,v)}$ ,  $q_m^{(l,v)}$  can be expressed as a function of  $a_m^{(l,v)}$ ,

$$\mathbf{q}^{(l,v)} = \mathbf{\Pi}^{(l,v)} \mathbf{a}^{(l,v)}, \quad (22)$$

where  $\mathbf{a}^{(l,v)} = [a_m^{(l,v)}]$ ,  $\mathbf{\Pi}^{(l,v)} = [\mathbf{I} - \mathbf{\Phi}^{(l,v)} \mathbf{R}^{l,l'}]^{-1} \mathbf{\Phi}^{(l,v)} \mathbf{T}^{l,l'}$ ,  $\mathbf{R}^{l,l'} = \text{diag} \{ R_m^{l,l'} \}$ ,  $\mathbf{T}^{l,l'} = \text{diag} \{ T_m^{l,l'} \}$ ,  $\mathbf{\Phi}^{(l,v)} = [\Phi_{m,n}^{(l,v)}]$ , and

$$\Phi_{m,n}^{(l,v)} = \sum_{u \in \mathbb{Z}} \bar{R}_u^{(l,v)} \varphi_{u-m}^J(k_f^l, \mathbf{o}^{(l,v)} - \bar{\mathbf{o}}^{(l,v)}) \varphi_{n-u}^J(k_f^l, \bar{\mathbf{o}}^{(l,v)} - \mathbf{o}^{(l,v)}). \quad (23)$$

From the above analysis, one can conclude that a circular inclusion can be equivalently modeled as a line source at the fiber center on condition that its CWE coefficient  $q_m^{(l,v)}$  satisfies Eq. (22).

Like equivalences are valid for the other concerned damages. For the displaced fiber, following an analysis similar with the one for the circular inclusion, the relation in Eq. (22) is obtained but with a different definition of  $\mathbf{\Pi}^{(l,v)}$ ,

$$\mathbf{\Pi}^{(l,v)} = (\mathbf{T}^l)^{-1} \left( \boldsymbol{\varphi}_1^{(l,v)} \mathbf{R}^l \boldsymbol{\varphi}_2^{(l,v)} - \mathbf{R}^l \right), \quad (24)$$

where  $\boldsymbol{\varphi}_1^{(l,v)} = [\boldsymbol{\varphi}_{n-m}^l(k_s^l, \mathbf{o}^{(l,v)} - \tilde{\mathbf{o}}^{(l,v)})]$ ,  $\boldsymbol{\varphi}_2^{(l,v)} = [\boldsymbol{\varphi}_{n-m}^l(k_s^l, \tilde{\mathbf{o}}^{(l,v)} - \mathbf{o}^{(l,v)})]$ ,  $\tilde{\mathbf{o}}^{(l,v)}$  being the center of the displaced fiber.

For the missing, expanded, shrunk fiber, one gets the corresponding definition of  $\mathbf{\Pi}^{(l,v)}$  by reformulating the linear relation of Eq. (7a). Since no fields are scattered by the missing fiber,  $b_m^{(l,v)} = 0$ . Then Eq. (7a) yields

$$q_m^{(l,v)} = -\frac{R_m^l}{T_m^l} a_m^{(l,v)}. \quad (25)$$

For the expanded and shrunk fiber, the CWE coefficients are related by

$$b_m^{(l,v)} = \tilde{R}_m^{(l,v)} a_m^{(l,v)}, \quad (26)$$

where  $\tilde{R}_m^{(l,v)}$  is similarly defined with  $R_m^l$  but with a different fiber radius. The rewritten form of Eq. (26),

$$b_m^{(l,v)} = R_m^l a_m^{(l,v)} + T_m^l \left[ \frac{1}{T_m^l} \left( \tilde{R}_m^{(l,v)} - R_m^l \right) \right] a_m^{(l,v)}, \quad (27)$$

leads to

$$q_m^{(l,v)} = \left[ \frac{1}{T_m^l} \left( \tilde{R}_m^{(l,v)} - R_m^l \right) \right] a_m^{(l,v)}. \quad (28)$$

Thus,  $\mathbf{\Pi}^{(l,v)}$  is defined as  $\text{diag} \left\{ -R_m^l / T_m^l \right\}$  for the missing fiber and  $\text{diag} \left\{ \left( \tilde{R}_m^{(l,v)} - R_m^l \right) / T_m^l \right\}$  for the expanded and shrunk fiber. The coefficient of  $q_m^{(l,v)}$  (or  $a_m^{(l,v)}$ ) needs to be solved to determine the equivalent source and get the field solution.

According to the scattering linearity about multiple sources, the field solution is decomposed as

$$V(\mathbf{r}) = V^{inc}(\mathbf{r}) + \sum_{(l,v) \in \mathbb{D}} \sum_{n \in \mathbb{Z}} q_n^{(l,v)} G_n(\mathbf{r}, \mathbf{o}^{(l,v)}). \quad (29)$$

where  $V^{inc}$  is the field solution w.r.t. the exterior source and  $G_n(\mathbf{r}, \mathbf{o}^{(l,v)})$  as the field response due to the cylindrical wave  $\boldsymbol{\varphi}_n^{H(1)}(k_j^l, \mathbf{r}_{(l,v)})$ , i.e., the field solution by setting  $q_m^{(l,v)} = \delta_{m,n}$  in Section 4. The second summed term in Eq. (29) is based on the CWE representation of the field scattered by the equivalent source  $\sum_{n \in \mathbb{Z}} q_n^{(l,v)} \boldsymbol{\varphi}_n^{H(1)}(k_j^l, \mathbf{r}_{(l,v)})$ .

The associated CWE coefficients of Eq. (29) have the similar relation,

$$a_m^{(l,v)} = a_{m,inc}^{(l,v)} + \sum_{(l,v) \in \mathbb{D}} \sum_{n \in \mathbb{Z}} q_n^{(l,v)} a_{m,n}^{(l,v)}. \quad (30)$$

The solution to  $a_{m,inc}^{(l,v)}$  and  $a_{m,n}^{(l,v)}$  is obtained during the computation of  $V^{inc}$  and  $G_n(\mathbf{r}, \mathbf{o}^{(l,v)})$ . The combination of Eq. (22) and Eq. (30) yields the solution of  $q_m^{(l,v)}$  as

$$\mathbf{q}^{\mathbb{D}} = \left( \mathbf{I} - \mathbf{\Pi}^{\mathbb{D}} \mathbf{\Lambda}^{\mathbb{D}} \right)^{-1} \mathbf{\Pi}^{\mathbb{D}} \mathbf{a}_{inc}^{\mathbb{D}}, \quad (31)$$

where the vector  $\mathbf{q}^{\mathbb{D}} = [q_m^{(l,v)}]$ ,  $\mathbf{a}_{inc}^{\mathbb{D}} = [a_{m,inc}^{(l,v)}]$  and matrix  $\mathbf{\Lambda}^{\mathbb{D}} = \text{diag} \left\{ \Lambda^{(l,v)} \right\}$ ,  $\Lambda^{(l,v)} = [a_{m,n}^{(l,v)}]$ ,  $\mathbf{\Pi}^{\mathbb{D}} = \text{diag} \left\{ \mathbf{\Pi}^{(l,v)} \right\}$ ,  $(l,v) \in \mathbb{D}$ . Finally, with the solution of  $q_m^{(l,v)}$ , the field solution is obtained by following Eq. (29).

Remark that, since only the coefficients of damaged fibers are concerned in Eq. (31) and the number of damaged fibers is usually small, the size of matrices in (31) is not large and the computational cost for the involved matrix inversion is low. Moreover, since  $V^{inc}$ ,  $G_n$ ,  $\mathbf{a}_{inc}^{\mathbb{D}}$ ,  $\Lambda^{\mathbb{D}}$  are only related with the structure of the undamaged laminate and the incident wave, which are usually known, these quantities can be computed in advance and stored.

## 6. Truncation of expansions

**Table 1. Numerical strategy to truncate PWE and CWE.**

1. Initialize the set of layer indexes  $\mathbb{L} = \{1, 2, \dots, L\}$ ,  $M_l = M_l^{\max}$ ,  $l \in \mathbb{L}$ ,  $P = 0$ , threshold  $\tau$ , and position of the observation points  $(x'_l, z'_l)$ ,  $x'_l = x_l^0$ ,  $z'_l = (z_l^0 + t_l)/2$ .
2. Compute field values at  $(x'_l, z'_l)$ ,  $l \in \mathbb{L}$ , by CWE and PWE and denote the field solution by  $V_c^l$  and  $V_p^l$ .
3. If  $\max\{|V_p^l - V_c^l|, l \in \mathbb{L}\} < \tau$ , go to step 4; otherwise, update  $P_l = P_l + 1$  and go to step 2.
4. Update  $M_l = M_l - 1$  for  $l \in \mathbb{L}$  and compute corresponding  $V_p^l$  and  $V_c^l$ .
5. If  $|V_p^l - V_c^l| \geq \tau$ ,  $l \in \mathbb{L}$ , update  $M_l = M_l + 1$  and  $\mathbb{L} = \mathbb{L} \setminus \{l\}$ . If  $\mathbb{L}$  is empty, stop; otherwise, go to step 4.

PWEs and CWEs are infinite series and approximated by truncations  $\sum_{p=-P}^P$  and  $\sum_{p=-M}^M$  in the computation. There is a trade-off in the selection of the truncation number  $P$  and  $M$ . Larger  $P$  and  $M$  lead to a higher computational cost (especially considering hundreds even thousands of computation of the integrand for numerical integrations, e.g. in Eq. (17)), while the modeling accuracy cannot be guaranteed with small values of  $P$  and  $M$ . Moreover, too large  $M$  may lead to ill-conditioned matrices, which are inverted during the computation of scattering matrices.

In the authors' previous work [7],  $P$  and  $M$  for the single-layer laminate are estimated by a numerical strategy which benefits from the knowledge that field values computed by PWE and CWE in the vicinity of fibers are the same. For multilayer structures, since the geometry and composing material might differ, optimal  $P$  and  $M$  might be changed accordingly from one layer to another. Thus, the numerical strategy is adjusted to fit the modeling of multilayer laminates. It is summarized in Table 1. Step 2 and 3 are to select  $P$ , the value for different layers being chosen to be the same to facilitate mode matching on slab boundaries. Step 4 and 5 aim at reducing  $M_l$ , which denotes the truncation number of CWE for the  $l$  layer, from its maximum value, which is set as  $M_l^{\max} = \text{Int}\left(\Re\left(4.05 \times (k_s^l c_l)^{1/3} + k_s^l c_l\right)\right) + 7$  [19], 7 being a security number. Parameter  $\tau$ , which determines the modeling accuracy, is a small positive constant. Remark that  $\tau$  cannot be too small in order to avoid too large  $P$  and  $M$ . Values from  $10^{-4}$  to  $10^{-3}$  seem to be robust and generate accurate enough field solution.

## 7. Numerical results

Truncation numbers  $P$  and  $M$  are first discussed with a 2-layer undamaged laminate. The material of the slab is with relative permittivity  $\epsilon_s^1, \epsilon_s^2 = 3.6 + i0.072$  and the fiber materials are with  $\epsilon_f^1 = 6$ ,  $\Re(\epsilon_f^2) = 12$ , conductivity  $\sigma_f^2 = 330$  S/m. The fiber period is  $d = 0.1$ mm and the thickness of each slab is  $d$ . Fibers are placed in the middle of each layer (i.e.,  $z^{(l,0)} = (t_l + t_{l+1})/2$ ) and no shift appears between the fiber arrays (i.e.,  $x^{(1,0)} = x^{(2,0)}$ ). The laminate is illuminated by a plane wave  $E^{inc} = e^{-i\alpha_0(z-d/2)}$ ,  $\alpha_0 = k_s^0 \sin \theta^{inc}$ ,  $\theta^{inc} = \pi/6$ , with the TE polarization. Setting

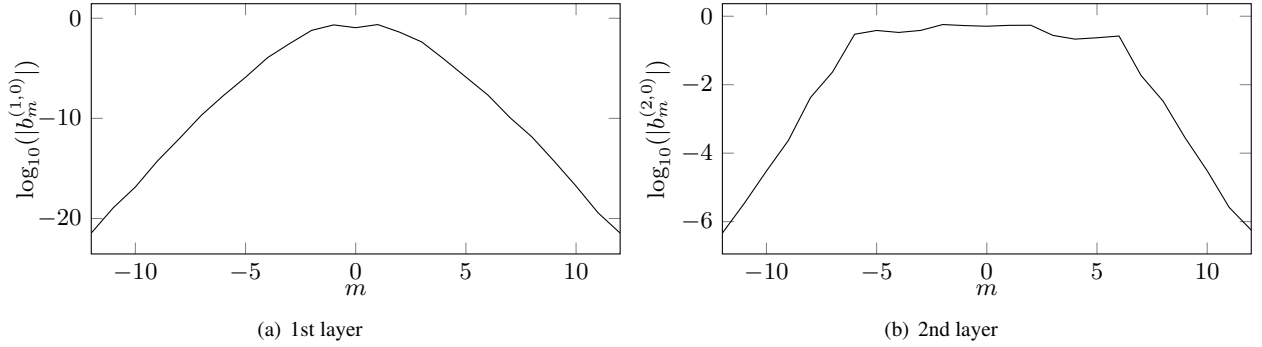


**Fig. 7.** Line graphs of CWE coefficients  $b_m$ ,  $M = 12$ , two-layer laminate with the plane-wave illumination,  $\theta^{inc} = \pi/6$ ,  $\lambda^{inc} = d$ .

$\tau = 10^{-3}$  in Table 1, the truncation scheme yields the selection value for  $P$  as 4,  $M_1 = 8$  and  $M_2 = 12$ . The value of  $M_2$  being larger than the one of  $M_1$  can be explained by observing the line graphs of CWE coefficients  $b_m^{(l,0)}$  (the coefficients of other fibers follow the Floquet theorem) in Fig. 7. While the absolute value of  $b_m^{(l,0)}$  decreases with  $|m|$ , since the radius of fibers in the second layer ( $c_2 = 0.4d$ ) is larger than that in the first layer ( $c_1 = 0.1d$ ), the decreasing rate of  $|b_m^{(1,0)}|$  is faster than  $|b_m^{(2,0)}|$ , which means that the field solution around the fibers in the first layer converges faster with  $M$ .

Validation of the proposed computational approach is performed with a 3-layer laminate sandwiched by air. Let the fiber period  $d = 0.1\text{mm}$ , radius  $c_l = (l + 1)d/10$ ,  $l = 1, 2, 3$ , and the origin of the local coordinates systems  $(x^{(l,0)}, z^{(l,0)})$  as  $z^{(l,0)} = (t_l + t_{l+1})/2$ ,  $t_l = 3d/2 - ld$ . Fiber arrays in 2nd and 3rd layers are shifted with  $x^{(2,0)} = 0.1d$ ,  $x^{(3,0)} = -0.1d$ . Fiber materials are with  $\epsilon_f^1, \epsilon_f^3 = 6$ ,  $\Re(\epsilon_f^2) = 12$ , conductivity  $\sigma_f^2 = 330 \text{ S/m}$ , while the slabs are slightly lossy (loss tangents of 0.02) with  $\epsilon_s^1, \epsilon_s^3 = 2.8 + i0.056$ ,  $\epsilon_s^2 = 3.6 + i0.072$ . Permeabilities  $\mu_j^l = 1$ ,  $j = s, f$ . The parameter  $\tau$  in Table 1 is set as  $10^{-4}$  to ensure the validation accuracy and the truncation number selected by the truncation scheme is  $P = 5$ ,  $M_1 = 10$ ,  $M_2 = 11$ ,  $M_3 = 13$ ,  $M_l$  the optimal  $M$  for the  $l$ -th layer.

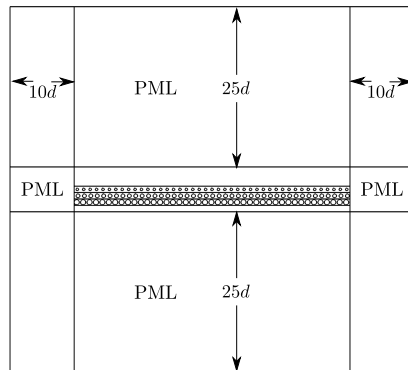


**Fig. 8.** Geometry of COMSOL module, 43 fibers in each layer of the laminate, fiber radius  $c_1 = 0.2d$ ,  $c_2 = 0.3d$ ,  $c_3 = 0.4d$ .

The solution to the Green's function is validated by comparisons with COMSOL, which is based on a finite element method, Fig. 8 shows the geometry of the COMSOL module which one uses, where 43 fibers are embedded in each layer. Perfect matching layers (PMLs) are used to simulate open boundaries. PMLs above and below the

laminate are chosen thicker than the others considering possibly strong reflections or transmissions.

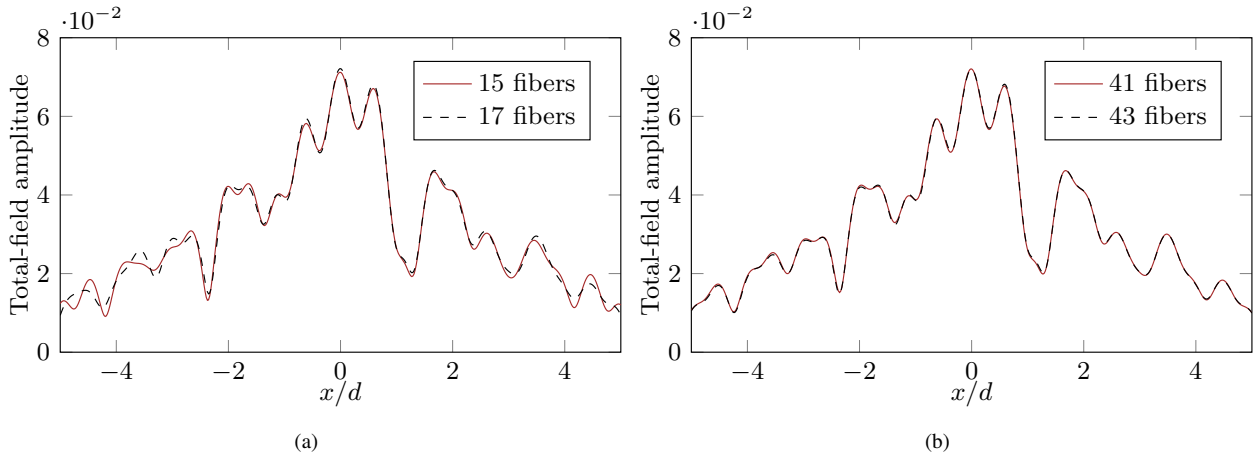


**Fig. 9.** Amplitude of sampled total fields vs number of fibers in COMSOL,  $\mathbf{r}_s = (0, 0)$ ,  $\lambda^{inc} = d$ ,  $z = d$ , TM polarization.

Set the line source at  $\mathbf{o}^{(1,0)}$  and run COMSOL with default mesh settings [20] (physics-controlled mesh with “Extremely fine” element size). Since scattered fields are often collected above the laminate, fields are sampled along the line  $-5d \leq x \leq 5d$ ,  $z = d$ , which is close to the laminate boundary so that evanescent components are counted in the validation. The number of fibers, 43, is decided by observing the convergence of the field solution. As shown in Fig. 9, with 41 fibers, adding one more fiber at each end of the laminate, the total-field solution generated by COMSOL has almost no differences. **In contrast, with 15 fibers, since the the fibers at the end of the laminate locate close to the emitting source and the sampling region, their scattering effects cannot be neglected and, as a consequence, significant differences are observed at tails when putting more fibers.** The field solution with TE polarization has a similar convergence.

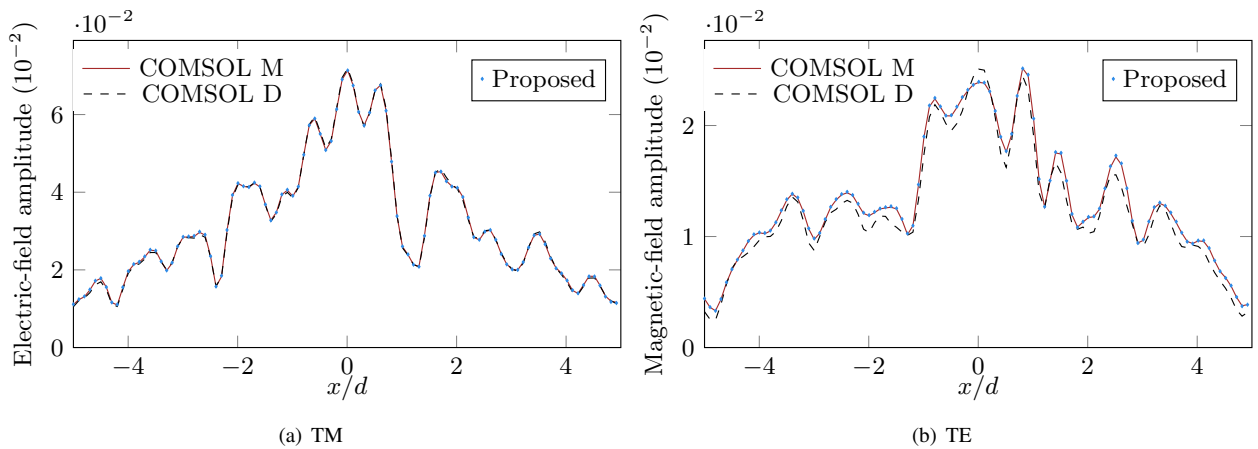


**Fig. 10.** Validation of the computation of the Green’s function by comparisons with COMSOL,  $\mathbf{r}_s = (0, 0)$ ,  $\lambda^{inc} = d$ ,  $z = d$ , “COMSOL D” denoting COMSOL solution with the default mesh settings and “COMSOL M” with manual settings.

The solution to the Green’s function computed by the presented approach is validated. As observed from Fig. 10,

with default mesh settings, although the field solution of the proposed approach fits COMSOL well with TM polarization, differences appear with TE polarization. The “maximum element growth rate”, the parameter in COMSOL determining the maximum rate at which the element size can grow [20], is then reduced from the defaulted 1.1 to 1.01 to have a finer mesh to more accurately represent the geometry. The field solution associated with this manual setting is denoted by “COMSOL M” in Fig. 10 and, as observed, fits well with the proposed approach. The reciprocity theorem is tested as well to check the modeling accuracy. Exchanging the position of source and observation points, the relative error  $\tau = |G(\mathbf{r}, \mathbf{r}_s) - G(\mathbf{r}_s, \mathbf{r})| / |G(\mathbf{r}, \mathbf{r}_s)|$ , is less than  $1.5 \times 10^{-8}$ .

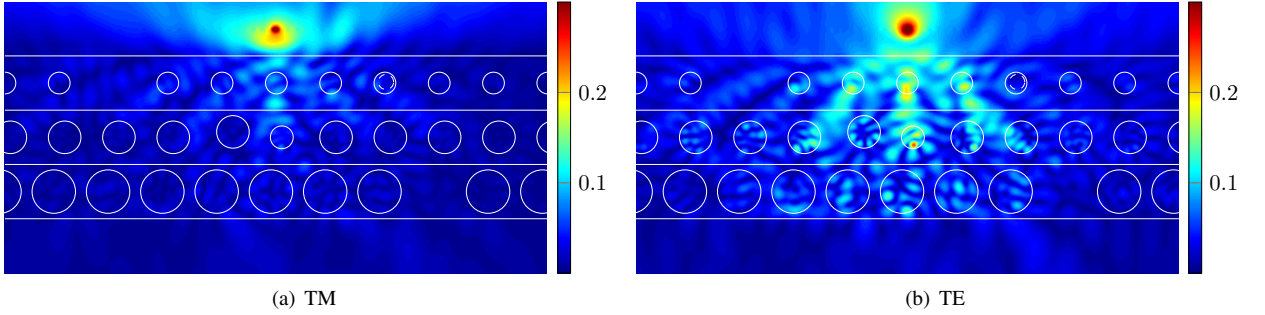


**Fig. 11. Amplitude of total (a) electric field and (b) magnetic field with a line-source illumination,  $\mathbf{r}_s = (0, d)$ ,  $\lambda^{inc} = d$ , white lines indicating the laminate structure.**

Now, assume all the kinds of mentioned damages exist in the laminate. Specifically, the  $(1, -3)$ -th and  $(3, 3)$ -th fibers are missing,  $\tilde{\mathbf{o}}^{(2,-1)} - \mathbf{o}^{(2,-1)} = (0.1d, 0.1d)$  for the displaced fiber,  $\tilde{c}^{(2,0)} = 0.7c_2$  for the shrunk fiber and  $\tilde{\mathbf{o}}^{(1,2)} - \mathbf{o}^{(1,2)} = (0.1c_1, 0.1c_1)$ ,  $\tilde{c}^{(1,2)} = 0.7c_1$  for the circular inclusion. A line source at  $\mathbf{r}_s = (0, d)$  illuminates this damaged laminate with the wave  $H_0^{(1)}(k_s^0 r_s)/(4i)$ ,  $r_s = |\mathbf{r} - \mathbf{r}_s|$ , wavelength  $\lambda^{inc} = d$ . In TM and TE polarizations, the distributions of total-field amplitudes are shown in Fig. 11, where the amplitude is limited at 0.3 for easier appraisal. In the TM case, most of the energy is reflected into the upper half space and little penetrates into the laminate, while more energy propagates inside in the TE case.

To validate the computational approach for modeling defects, 500 values are respectively sampled along the line  $z = 0$ ,  $-5d \leq x \leq 5d$  and the line  $z = -d$ ,  $-5d \leq x \leq 5d$ . The comparisons with results from COMSOL are shown in Fig. 12. Two solutions again are generated by COMSOL with default mesh settings and manual settings (maximum element growth rate changed as 1.01), respectively. Slight differences appear among the three solutions. However, the fields computed by the proposed approach is between the two COMSOL solutions for most points, despite strong fluctuations due to the size of component, i.e., slab thickness and fiber radius, close to the wavelength.

When the wavelength is much larger than the component size, the field inside the fiber should only be slightly impacted by the damages and the Born approximation can be used as described in Appendix B. With the same composite but setting  $\lambda^{inc} = 100d$  and assuming only missing fibers exist, the comparison of computed anomalous field is shown in Fig. 13. The peak value appears at the position corresponding to the  $(3, 3)$ -th missing fiber due to its larger radius ( $c_3 = 0.4d$  while  $c_1 = 0.2d$ ).

The modeling efficiency is indicated by Table 2, which presents the computational time of reaching line graphs

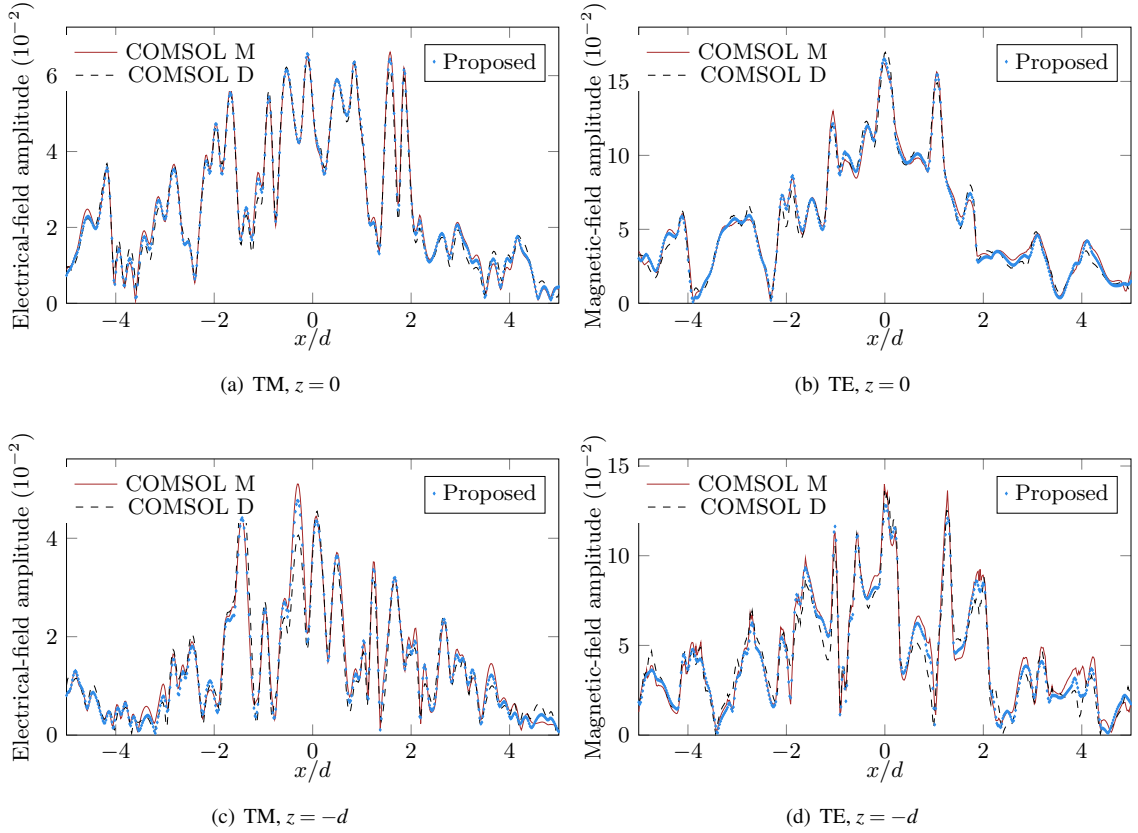


**Fig. 12. Validation of modeling the damaged laminate through comparisons with COMSOL,  $\mathbf{r}_s = (0, d)$ ,  $\lambda^{inc} = d$ , “COMSOL D” denoting COMSOL solution with the default mesh settings and “COMSOL M” with manual settings.**

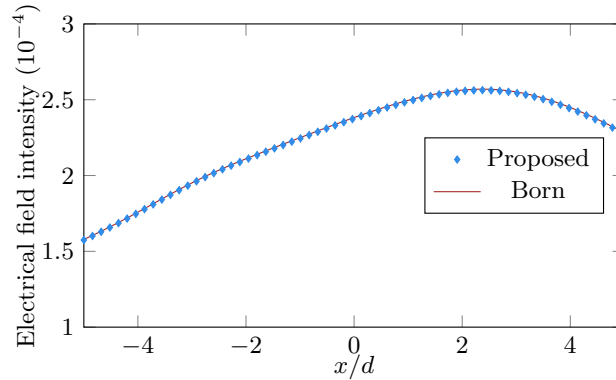


**Fig. 13. Anomalous field computed by the proposed approach and the Born approximation, the (1, -3)-th and (3, 3)-th fibers are missing,  $\mathbf{r}_s = (0, d)$ ,  $\lambda^{inc} = 100d$ , TM,  $z = 1.5d$ .**

in Fig. 10(a), 10(b), 12(a) and 12(b) on a laptop (dual cores, clock speeds 2.6 GHz, memory 16 GB). The solution of the Green’s function in Fig. 10(a) and 10(b) costs less than 16 seconds with the proposed approach. However, as mentioned in Section 5, the computational time for the Green’s function can be saved, since it is not related with defects and thus can be computed in advance and stored. Computing the quantities of  $V^{inc}$ ,  $G_n$ ,  $\mathbf{a}_{inc}^D$ ,  $\Lambda^D$  in advance, the

**Table 2. Comparison of computation time (in seconds)**

	Fig. 10(a)	Fig. 10(b)	Fig. 12(a)	Fig. 12(b)
COMSOL D	20	18	16	18
COMSOL M	53	130	86	96
Proposed	11	15	0.26	0.23

efficiency for modeling the concerned damaged laminates is high and the computation of line graph by the proposed approach in Fig.12(a) and 12(b) costs 0.26s and 0.23s, respectively. In contrast, COMSOL needs much more time to reach approximated solutions.

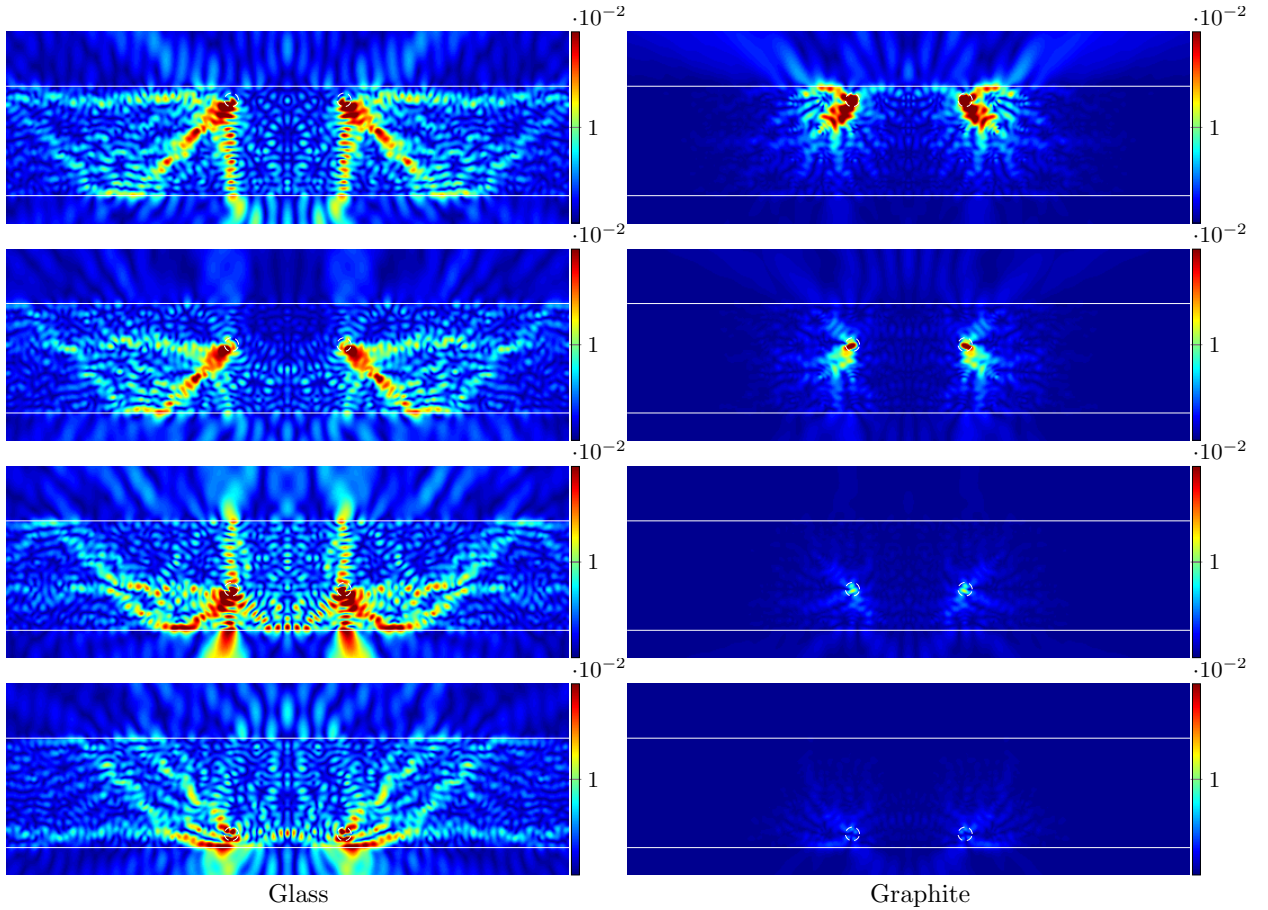


**Fig. 14. Maps of anomalous field with the  $(l, 2)$ -th and  $(l, 2)$ -th fibers missing,  $l = 1, 2, 3, 4$ , line source at  $(0, d)$ ,  $\lambda^{inc} = d$ , TM.**

Challenges in imaging are numerous. Generally, sources and receivers can only be put above the laminate in the testing system to collect the information. Yet, for the damages inside deep layers, their impacts on the scattered field might be reduced significantly due to losses and, therefore, these damages should not be easily identified. Investigations here are led on a 4-layer laminate by moving the missing fibers from layer to layer. Each layer of the laminate enjoys the same structure and composition. Maps of anomalous field are found in Fig. 14, where only amplitudes smaller than 0.02 are displayed for better appraisal. With graphite fibers and epoxy slabs, due to lossy fibers, the

amplitude of the anomalous field in the upper half space significantly reduces as the missing fibers move deeper and deeper. When the missing fibers show up at the bottom layer, one has almost no hint of damages when above the laminate. However, changing the fiber material to lossless glass, as shown in the left figures of Fig. 14, the field decays much slower in the propagation. As a result, the impacts of damages can be observed above the laminate even if the missing fibers are located in the bottom layer.

## 8. Conclusion

The modeling of damaged periodic fibered laminates and the solution to the associated Green's function are the topics of concern herein. Modeling the undamaged laminates by computing the scattering matrices with a recursive scheme, the solution to the Green's function is obtained with the array scanning method, where the hypothesized phased array is first analyzed with the quasi-periodic theory and the final solution follows from integration over the first Brillouin zone. The field disturbance by missing, displaced, shrunk, and expanded fibers and circular inclusions is modeled as equivalent sources. According to the scattering linearity, the field solution to the damaged laminate is a summation of responses due to the exterior illuminating source and equivalent ones. The proposed modeling approach is validated by comparing results from COMSOL or the Born approximation.

Circular damages associated with fibers are those concerned in this contribution. For damages within a slab but outside fibers, the equivalence theory is to applied and solving the corresponding Green's function is the first step. For defects with arbitrary shapes, a method of moments within a proper field integral formulation can apply. **The direct modeling of twisted (instead of straight) fibers, which are randomly distributed in the background slab, is another strong challenge ahead of the authors.**

Behaviors of photonic crystals may be analyzed with the equivalence theory due to similar structures. For instance, the so-called defect mode may be observed by selecting frequencies for a singular matrix in Eq. (31) [21].

## Appendix A. Some variable definitions

In (2),  $\mathcal{E}_l^u$ ,  $u = 1, 2, 3, 4$ , are defined as the diagonal matrix of  $\mathcal{E}_l^{u,p}$  and

$$\begin{aligned}\mathcal{E}_{l,p}^1 &= \frac{2w_p^{l-1} e^{i\alpha_p(x_l-x_{l-1})} e^{i[\beta_p^l(t_{l-1}-z_l)-\beta_p^{l-1}(t_{l-1}-z_{l-1})]}}{w_p^{l-1} + w_p^l} \\ \mathcal{E}_{l,p}^2 &= \frac{-(w_p^{l-1} - w_p^l) e^{i2\beta_p^l(t_{l-1}-z_l)}}{w_p^{l-1} + w_p^l} \\ \mathcal{E}_{l,p}^3 &= \frac{(w_p^{l-1} - w_p^l) e^{-i2\beta_p^{l-1}(t_{l-1}-z_{l-1})}}{w_p^{l-1} + w_p^l} \\ \mathcal{E}_{l,p}^4 &= \frac{2w_p^l e^{-i\alpha_p(x_l-x_{l-1})} e^{i[\beta_p^l(t_{l-1}-z_l)-\beta_p^{l-1}(t_{l-1}-z_{l-1})]}}{w_p^{l-1} + w_p^l}\end{aligned}$$

where  $w_p^l = \beta_p^l / (\mu_0 \mu_s^l)$  for TM and  $w_p^l = \beta_p^l / (\epsilon_0 \epsilon_s^l)$  for TE,  $\mu_0$ ,  $\epsilon_0$  the permeability and permittivity of air.

$R_m^l, T_m^l, R_m^{l'}, T_m^{l'}$  in (7a) and (7b) are defined as

$$\begin{aligned} R_m^l &= \frac{\eta_s^l J_m(k_s^l c_l) J_m(k_j^l c_l) - \eta_f^l J_m(k_s^l c_l) J_m(k_j^l c_l)}{\eta_f^l J_m(k_j^l c_l) \dot{H}_m^{(1)}(k_s^l c_l) - \eta_s^l J_m(k_j^l c_l) H_m^{(1)}(k_s^l c_l)}, \\ T_m^l &= \frac{2i\eta_s^l}{\pi c_l k_j^l} \frac{1}{\eta_f^l J_m(k_j^l c_l) \dot{H}_m^{(1)}(k_s^l c_l) - \eta_s^l J_m(k_j^l c_l) H_m^{(1)}(k_s^l c_l)}, \\ R_m^{l'} &= \frac{\eta_s^l H_m^{(1)}(k_s^l c_l) \dot{H}_m^{(1)}(k_j^l c_l) - \eta_f^l \dot{H}_m^{(1)}(k_s^l c_l) H_m^{(1)}(k_j^l c_l)}{\eta_f^l J_m(k_j^l c_l) \dot{H}_m^{(1)}(k_s^l c_l) - \eta_s^l J_m(k_j^l c_l) H_m^{(1)}(k_s^l c_l)}, \\ T_m^{l'} &= \frac{2i\eta_f^l}{\pi c_l k_s^l} \frac{1}{\eta_f^l J_m(k_j^l c_l) \dot{H}_m^{(1)}(k_s^l c_l) - \eta_s^l J_m(k_j^l c_l) H_m^{(1)}(k_s^l c_l)}. \end{aligned}$$

for TM, where  $\eta_s^l$  and  $\eta_f^l$  are characteristic impedances of the slab and sound fiber within the  $l$ -th layer, dots above letters standing for the differential operator. Exchanging positions of  $\eta_f^l$  and  $\eta_s^l$  generates the TE formulas.

## Appendix B. Application of the Born approximation

With missing fibers, the field disturbance can be valued by the Fredholm integral equation [22]

$$\tilde{V}(\mathbf{r}) - V(\mathbf{r}) = \sum_{(l,v) \in \mathbb{D}} \int_{D^{(l,v)}} G(\mathbf{r}, \mathbf{r}'_s) \left[ (k_j^l)^2 - (k_s^l)^2 \right] \tilde{V}(\mathbf{r}'_s) d\mathbf{r}'_s, \quad (\text{B.1})$$

where  $D^{(l,v)}$  is the cross-section of the  $(l, v)$ -th fiber,  $V$  is the field solution for the sound laminate and  $\tilde{V}$  for the damaged one. With large wavelengths,  $\tilde{V}(\mathbf{r}'_s) \approx V(\mathbf{r}'_s)$ , thus

$$\tilde{V}(\mathbf{r}) - V(\mathbf{r}) \approx \sum_{(l,v) \in \mathbb{D}} \int_{D^{(l,v)}} G(\mathbf{r}, \mathbf{r}'_s) \left[ (k_j^l)^2 - (k_s^l)^2 \right] V(\mathbf{r}'_s) d\mathbf{r}'_s. \quad (\text{B.2})$$

Denote  $g_p^0$  as the PWE coefficients for  $G$  when the observation point is above the laminate and  $C_m^{(l,v)}$  as the CWE coefficients for  $V(\mathbf{r}'_s)$ . Substituting the expression of  $G$  and  $V$  into the integrand, Eq. (B.2) is rewritten as

$$\tilde{V}(\mathbf{r}) - V(\mathbf{r}) = \frac{d}{4i} \int_{-\pi/d}^{\pi/d} \sum_{(l,v) \in \mathbb{D}} \sum_{m \in \mathbb{Z}} \Phi_m^{(l,v)}(\alpha_0) C_m^{(l,v)} d\alpha_0, \quad (\text{B.3})$$

where  $\Phi_m^{(l,v)}$  is the  $m$ -th column of  $\Phi^{(l,v)}$ ,

$$\Phi^{(l,v)} = \Gamma^{(l,v)} \mathcal{D}_0^{l+} \frac{\Theta_{l+} \mathcal{E}_{l-}^{L+1} \Psi_l^{-1} \Omega^{l-} + \Omega^{l+}}{\mathcal{E}_l - \Theta_{l+} \mathcal{E}_{l-}^{L+1} \Psi_l^{-1} \Theta_{l-} \mathcal{B}_0^{l+}} \mathbf{T}^l \mathbf{J} \quad (\text{B.4})$$

where  $\Gamma^{(l,v)} = \left[ e^{i(\alpha_p(x-vd) + \beta_p^0(z-t_1))} \right]$  and  $\mathbf{J} = \text{diag} \left\{ k_f^l c_l J_{m+1}(k_f^l c_l) J_m(k_s^l c_l) - k_s^l c_l J_m(k_f^l c_l) J_{m+1}(k_s^l c_l) \right\}$ . The integration in (B.3) is computed by numerical methods.

## References

- [1] H. Heuer, M. Schulze, M. Pooch, S. Gäbler, A. Nocke, G. Bardl, C. Cherif, M. Klein, R. Kupke, R. Vetter, F. Lenz, M. Kliem, C. Bülow, J. Goyvaerts, T. Mayer, S. Petrenz, Review on quality assurance along the CFRP value chain – Non-destructive testing of fabrics, preforms and CFRP by HF radio wave techniques, *Compos. Part B - Eng.* 77 (2015) 494–501.
- [2] R. Zoughi, *Microwave Non-Destructive Testing and Evaluation Principles*, Springer Science & Business Media, Berlin, 2012.

- [3] C. Li, D. Lesselier, Y. Zhong, Full-wave computational model of electromagnetic scattering by arbitrarily rotated 1-D periodic multilayer structure, *IEEE Trans. Antennas Propag.* 64 (2016) 1047–1060.
- [4] K. Yasumoto, *Electromagnetic Theory and Applications for Photonic Crystals*, CRC Press, Boca Raton, 2005.
- [5] J. Wang, B. Zhou, L. Shi, C. Gao, B. Chen, Efficiency-improved LOD-FDTD method for solving periodic structures at oblique incidence, *IEEE Microw. Wireless Compon. Lett.* 23 (2013) 521–523.
- [6] J. Tyrus, M. Gosz, E. DeSantiago, A local finite element implementation for imposing periodic boundary conditions on composite micromechanical models, *Int. J. Solids Struct.* 44 (2007) 2972–2989.
- [7] Z. Liu, C. Li, D. Lesselier, Y. Zhong, Electromagnetic modeling of damaged single-layer fiber-reinforced laminates, *IEEE Trans. Antennas Propag.* 65 (2017) 1855–1866.
- [8] Z. Liu, C. Li, D. Lesselier, Y. Zhong, Fast full-wave analysis of damaged periodic fiber-reinforced laminates, *IEEE Trans. Antennas Propag.* 66 (2018) 3540–3547.
- [9] F. Capolino, D. R. Jackson, D. R. Wilton, Fundamental properties of the field at the interface between air and a periodic artificial material excited by a line source, *IEEE Trans. Antennas Propag.* 53 (2005) 91–99.
- [10] C. Li, D. Lesselier, Y. Zhong, Recursive matrix schemes for composite laminates under plane-wave and Gaussian beam illumination, *J. Opt. Soc. Am. B* 32 (2015) 1539–1549.
- [11] J. Yang, L.-W. Li, K. Yasumoto, C.-H. Liang, Two-dimensional scattering of a Gaussian beam by a periodic array of circular cylinders, *IEEE Trans. Geosci. Remote Sens.* 43 (2005) 280–285.
- [12] K. Watanabe, Y. Nakatake, J. Pištora, Accurate analysis of electromagnetic scattering from periodic circular cylinder array with defects, *Opt. Express* 20 (2012) 10646–10657.
- [13] L. C. Botten, N.-A. P. Nicorovici, A. A. Asatryan, R. C. McPhedran, C. M. de Sterke, P. A. Robinson, Formulation for electromagnetic scattering and propagation through grating stacks of metallic and dielectric cylinders for photonic crystal calculations. Part I. Method, *J. Opt. Soc. Am. A* 17 (2000) 2165–2176.
- [14] S. Wilcox, L. Botten, R. McPhedran, C. Poulton, C. M. de Sterke, Modeling of defect modes in photonic crystals using the fictitious source superposition method, *Phys. Rev. E* 71 (2005) 056606.
- [15] M. Abramowitz, I. A. Stegun, *Handbook of Mathematical Functions: with Formulas, Graphs, and Mathematical Tables*, Dover Publications, New York, 1965.
- [16] K. Yasumoto, K. Yoshitomi, Efficient calculation of lattice sums for free-space periodic Green's function, *IEEE Trans. Antennas Propag.* 47 (1999) 1050–1055.
- [17] R. Denlinger, Z. Gimbutas, L. Greengard, V. Rokhlin, A fast summation method for oscillatory lattice sums, *J. Math. Phys.* 58 (2017) 023511.
- [18] P. Gonnet, Increasing the reliability of adaptive quadrature using explicit interpolants, *ACM Trans. Math. Software* 37 (2010) 26.
- [19] J.-P. Groby, A. Wirgin, L. De Ryck, W. Lauriks, R. Gilbert, Y. Xu, Acoustic response of a rigid-frame porous medium plate with a periodic set of inclusions, *J. Acoust. Soc. Am.* 126 (2009) 685–693.
- [20] *Introduction to COMSOL Multiphysics® v5.3*, COMSOL Multiphysics, Burlington, 2017.
- [21] R. Faggiani, A. Baron, X. Zang, L. Lalouat, S. A. Schulz, B. O'Regan, K. Vynck, B. Cluzel, F. De Fornel, T. F. Krauss, L. Philippe, Lower bound for the spatial extent of localized modes in photonic-crystal waveguides with small random imperfections, *Sci. Rep.* 6 (2016) 27037.
- [22] J.-P. Groby, D. Lesselier, Localization and characterization of simple defects in finite-sized photonic crystals, *J. Opt. Soc. Am. A* 25 (2008) 146–152.